



Significant enhancement of photocatalytic performance by constructing porous g-C₃N₄ composed of nanosheets

Tianran Hao¹ · Shiping Sun^{1,2} · Hongliang Xu¹ · Han Yu¹ · Wenbo Cao¹ · Gang Shao¹ · Bingbing Fan¹ · Hailong Wang¹ · Hongxia Lu¹

Received: 9 February 2023 / Accepted: 7 May 2023 / Published online: 18 May 2023

© The Author(s), under exclusive licence to Springer Nature B.V. 2023

Abstract

Porous g-C₃N₄ composed of nanosheets (p-gCN-NS) was synthesized through firstly grinding the hydrochloric acid-treated melamine with ammonium chloride (NH₄Cl) and then calcining the mixture at 550° C for 2 h. The photocatalytic properties were determined by degrading Rhodamine B (RhB) and tetracycline (TC) aqueous solution (10 mg/L, 100 mL). Results show that the crystallinity, size and thickness of g-C₃N₄ in p-gCN-NS reduced dramatically compared with those in g-C₃N₄ sample synthesized without the addition of NH₄Cl (gCN). Specific surface area of p-gCN-NS was 63.65 m²·g⁻¹, which was 6.7 times that of gCN. After photocatalysis for 50 min, the degradation rate of RhB achieved 99.32% by p-gCN-NS (100 mg), whose reaction rate constant ($k = 0.09317 \text{ min}^{-1}$) was 10.6 times higher than that of gCN. p-gCN-NS also exhibited excellent photocatalytic activity for degrading colorless tetracycline aqueous solution. The significant improvement of photocatalytic performance can be credited to the reduced sized and thickness of g-C₃N₄, higher specific surface area and pore structure, as well as the weakened recombination rate of photogenerated electron–hole pairs in p-gCN-NS. This work provides a feasible and facile method for synthesis porous g-C₃N₄ composed of nanosheets with excellent photocatalytic performance.

Keywords Porous g-C₃N₄ · Nanosheets · Preparation · Photocatalytic activity

✉ Hongliang Xu
xhlxhl@zzu.edu.cn

¹ School of Materials Science and Engineering, Zhengzhou University, No. 100, Science Avenue, Zhengzhou 450001, People's Republic of China

² Qinghai Institute of Salt Lakes, Chinese Academy of Science, Xining, Qinghai 810008, People's Republic of China

Introduction

Modernization of industry and human activities have caused some energy and environmental problems, including the dye pollution problem, which threatens the health of human beings and water living organisms [1, 2]. Many efforts have been tried to deal with this problem, including physical and biological technology [3], etc. As a green technology, photocatalytic technique is helpful to settle many energy and environmental problems, especially in the field of treating dye wastewater due to its low cost, low energy consumption, no by-products and mild reaction [4]. The types of photocatalyst materials are numerous, such as titanium dioxide (TiO_2), zinc oxide (ZnO) and cadmium sulfide (CdS). TiO_2 is the most commonly used commercial photocatalyst up to now [5]. However, due to its large band gap (3.2 eV), TiO_2 only responds to ultraviolet light, which impedes its widespread applications [6, 7]. Hence, many scientists are dedicated to synthesizing the high-efficient photocatalysts response to visible light.

In recent years, graphitic carbon nitride ($\text{g-C}_3\text{N}_4$), a metal-free polymeric semiconductor with a suitable band gap (2.7 eV) [8], has attracted much attention among researchers by virtue of its chemical and thermal stability, visible light response, non-toxicity, tunable electronic structure and powerful antioxidant. $\text{g-C}_3\text{N}_4$ photocatalyst has a wide range of applications, including water splitting [9], CO_2 reduction [10, 11], electrocatalyst [12], selective oxidation of alcohols [13] and organic pollutants degradation [14]. However, the photocatalytic performance of bulk $\text{g-C}_3\text{N}_4$ is poor, which is ascribed to the slow transfer rate of the charge carriers, high recombination rate of photogenerated electron–hole pairs, insufficient visible light absorption and low specific surface area (SSA) [15]. In order to solve these problems, many strategies have been carried out, including morphology design [16], chemical element doping [17, 18], construction of heterojunction structure [19], band gap engineering [20, 21], defect modification [22] and deposition of noble metal nanoparticles [23] or carbon materials [24].

Morphology control is an efficient method of improving the photocatalytic performance of $\text{g-C}_3\text{N}_4$, including $\text{g-C}_3\text{N}_4$ of nanosheets [23, 25], nanotubes [26, 27] and nanorods [28]. Till now, plenty of efforts have been put in the fabrication of $\text{g-C}_3\text{N}_4$ nanosheets, mainly including NH_3 etching [29], liquid exfoliation [12, 30], hydrothermal treatment [31], thermal etching [32, 33] and calcination melamine with ammonium chloride [34–36]. $\text{g-C}_3\text{N}_4$ nanosheet presents an enhanced photocatalytic property, owing to a larger special specific surface and more surface reactive sites offered by nanosheet structure of $\text{g-C}_3\text{N}_4$, which reduces the charge transfer distance and suppress the recombination of photogenerated charge carriers. In addition, porous $\text{g-C}_3\text{N}_4$ exhibits outstanding photocatalytic activity due to its large specific surface area and porous structure. Hence, it may be conducive to the improvement of photocatalytic performance by constructing a porous structure.

For the constructing of porous structure, the conventional template method possesses many shortcomings, such as cumbersome steps of removing silica nanoparticles template and more cost on preparation [37, 38]. On the contrary,

inorganic ammonium salt like ammonium chloride (NH_4Cl) can turn into gas during the calcination process. Therefore, NH_4Cl can be used as a gas bubble template agent, which is helpful to produce porous $\text{g-C}_3\text{N}_4$. In addition, the specific surface area and photocatalytic activity of $\text{g-C}_3\text{N}_4$ could be dramatically improved through pre-treating melamine with hydrochloride acid [39]. Consequently, the above two methods had been employed simultaneously to prepare porous $\text{g-C}_3\text{N}_4$ composed of nanosheets in this work, aiming to further improve the photocatalytic performance of $\text{g-C}_3\text{N}_4$.

Experimental section

Materials

Melamine (99%) and ammonium chloride (NH_4Cl , 99.5%) were acquired from Sinopharm Chemical Reagent Co., Ltd. Concentrated hydrochloric acid (HCl , 37%) was purchased from Luoyang Haohua Chemical Reagent Co., Ltd. Rhodamine B (RhB) and tetracycline hydrochloride (96%) were commercially available from Tianjin Kemiou Chemical Reagent Co., Ltd. and Shanghai Aladdin Bio-Chem Technology Co., Ltd., respectively. Deionized water was utilized in the study.

Preparation of porous $\text{g-C}_3\text{N}_4$ nanosheets and $\text{g-C}_3\text{N}_4$ particles

Porous $\text{g-C}_3\text{N}_4$ composed of nanosheets (p-gCN-NS) was prepared from melamine which was pre-treated by HCl aqueous solution and then calcined with NH_4Cl . In detail, a certain amount of melamine particles and 200 mL of HCl aqueous solution (4 mol/L) were mixed and magnetically stirred at 25 °C for 2 h, then centrifugally separated at 7000 r/min and dried at 60 °C, by which the acid-treated melamine was obtained. Then, 2 g of acid-treated melamine and 5 g of NH_4Cl were ground together for 30 min to mix them uniformly. Subsequently, the mixture was put into an alumina crucible, sealed with tin foil and placed into a tube furnace. It was heated up to 550 °C with a heating rate of 5 °C·min⁻¹ and then kept for 2 h in air. After cooling to ambient temperature, the obtained yellow solid substance was ground into powder in an agate mortar, washed with distilled water and dried at 60 °C for 12 h, which was denoted as p-gCN-NS.

Similarly, $\text{g-C}_3\text{N}_4$ particles (gCN) were prepared without the addition of NH_4Cl .

Characterization

The phase composition and crystal structure of samples were characterized by a Smart Lab X-ray diffractometer (XRD, Rigaku Corp., Japan) under the testing conditions of $\text{Cu K}\alpha$ radiation ($\lambda=0.15406$ nm) and the scanning rate of 4°·min⁻¹. The microstructure of samples were observed by a JSM 6701F field emission scanning electron microscope (SEM, JOEL, Tokyo, Japan) and a FEI Talos F200s transmission electron microscopy (TEM, FEI, Hillsboro, USA). Atomic force microscope (AFM) images

were obtained in tapping mode on a Bruker Multi Mode 8 AFM (Bruker, USA). The functional groups of samples were studied by a Nicolet iS10 Fourier transform infrared spectrometer (FT-IR, Thermo Fisher Scientific Corp., Massachusetts, USA). The UV–Vis adsorption spectra was detected by an UV-1800PC UV–visible spectrometer (Shanghai United States spectrum of Instrument Co., Ltd, China). SSA and the nitrogen adsorption and desorption isotherm of the samples were tested at 77 K using a Micromeritics ASAP 2460 apparatus (Micromeritics Instrument Corp., Atlanta, USA). The UV–Vis diffuse reflectance absorption spectra of the samples were measured using a Shimadzu UV-3600 spectrophotometer (Shimadzu Corp., Japan) stocked with a diffuse reflectance accessory, and BaSO₄ was used as the reference. X-ray photoelectron spectroscopy (XPS) was collected using an ESCALAB 250 spectrometer (Thermo Scientific Ltd., England) with focused monochromatized Al K α radiation. The photoluminescence (PL) spectra of the samples were measured by a Hitachi F-7000 fluorescence spectrometer (Tokyo, Japan) under the excitation of incident light of 365 nm at ambient temperature.

Evaluation of photocatalytic activity

The photocatalytic degradation of the RhB aqueous solution was performed at room temperature using a 300 W Xe Lamp with a 400 nm cutoff filter. First, 100 mg gCN or p-gCN-NS samples were put into the RhB solution (10 mg/L, 100 ml). Then, the suspension was stirred for 1 h in dark to reach an adsorption–desorption equilibrium. Then, the suspension was irradiated by the Xe Lamp under magnetic stirring and 4 mL of the suspension were sampled at a given time interval. Next, the photocatalyst particles were separated by centrifugation of the liquid samples at the speed of 10,000 r/min for 10 min. The RhB concentration of supernatant was analyzed by measuring the absorption intensity at 554 nm at the UV–Vis absorption spectra. According to the primary absorbance of RhB solution as well as the remnant absorbance of RhB solution after photocatalysis for different time, the photodegradation of RhB by photocatalyst could be calculated according to formula (1) [40]:

$$R = (1 - C/C_0) \times 100\% \quad (1)$$

Here, R is the photodegradation rate, and C_0 and C represent the initial RhB concentration and the residual RhB concentration after reaction time t , respectively.

The photocatalytic activity of the as-prepared photocatalyst samples toward degrading the colorless tetracycline aqueous solution was carried out utilizing the similar method stated above.

Results and discussion

XRD and IR analysis

XRD patterns of gCN and p-gCN-NS are shown in Fig. 1. The pattern of gCN presented (100) and (002) diffraction peaks of g-C₃N₄ at 2θ of 13.1 and 27.4°,

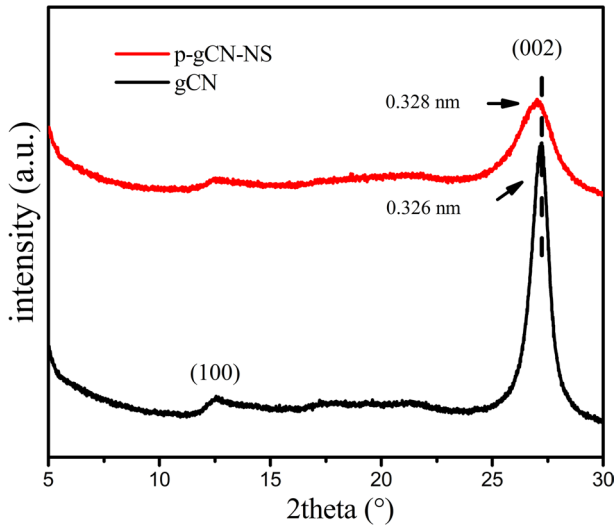


Fig. 1 XRD patterns of gCN and p-gCN-NS samples

respectively. The former is attributed to the inter-planar structural packing motif, and the latter can be ascribed to the inter-layer accumulation of the aromatic segments [41–44].

The XRD pattern of p-gCN-NS is similar to that of gCN, implying that they have the same crystal structure as g-C₃N₄. Nevertheless, compared with gCN, the intensity of (002) diffraction peak of p-gCN-NS was obviously reduced and the full width of half peak was widened. Moreover, the d_{002} value of g-C₃N₄, which were calculated by Bragg equation, changes from 0.326 nm for gCN to 0.328 nm for p-gCN-NS. The results show that the crystallinity and thickness of g-C₃N₄ in p-gCN-NS sample had a reduction, and its grain size decreased. This variation could be ascribed to the gas bubble, act as a gas template, produced by the thermal decomposition of NH₄Cl during the calcination of p-gCN-NS sample. In the light of the references [35, 45, 46], it can be inferred that the g-C₃N₄ nanosheets may be successfully prepared. Furthermore, the intensity of (100) diffraction of p-gCN-NS had a significant decrease and the peak shape become wider, which may be due to the destruction of inter-layer structural packing motif during the preparation process.

FT-IR spectra of gCN and p-gCN-NS are presented in Fig. 2. In the gCN spectrum, the bands at 3000–3500 cm⁻¹ can be attributed to the stretching vibrations of -NH₂, =NH groups and O-H bond [47]. The bands with wave numbers between 1200 and 1700 cm⁻¹ are assigned to the stretching vibrations of conjugated heterocyclic CN rings. The vibration of aromatic C=N occurred at 1563 and 1417 cm⁻¹, and the band at 1645 cm⁻¹ was ascribed to the vibration of C=O bond. The band at the wave number of 810 cm⁻¹ derived from the breathing vibration of triazine ring [41, 48]. p-gCN-NS possessed the same functional groups as gCN did, which is due to the similar IR spectra. Compared with gCN, the transmittance of the 810 cm⁻¹ band of p-gCN-NS was significantly lower, but the bands in the range of

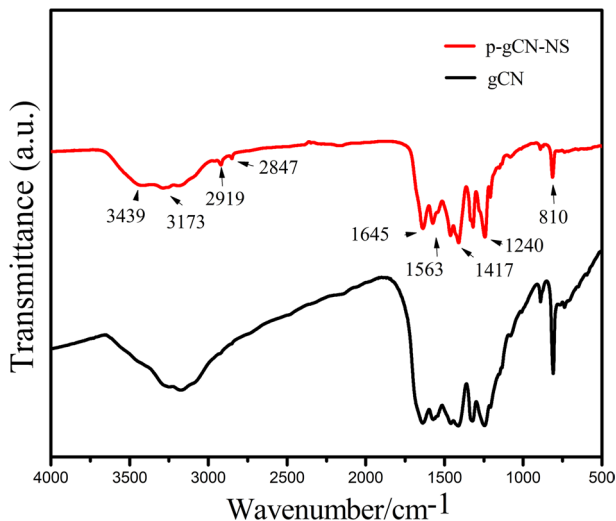


Fig. 2 Infrared spectra of gCN and p-gCN-NS samples

1200–1700 cm^{-1} of p-gCN-NS become stronger, stemming from the more ordered packing of tri-*s*-triazine motifs in the nanosheet layer [41, 47, 49]. Additionally, the bands at 2919, 2847 cm^{-1} can be assigned to the alkyl C–H stretching [48].

Microstructure analysis

Figure 3 provides the SEM and TEM images of gCN and p-gCN-NS. The size of the $\text{g-C}_3\text{N}_4$ particles in gCN sample were about 9 μm (Fig. 3a). Nevertheless, there were many $\text{g-C}_3\text{N}_4$ aggregates with the size of 200–300 nm, which were made up of irregular nanosheets and pores (Fig. 3b). Obviously, the microstructure of p-gCN-NS was significantly different from that of gCN. TEM photographs prove that irregular thick particle presented in gCN sample (Fig. 3c), but graphene-like morphology was observed in p-gCN-NS sample (Fig. 3d). This result indicates that the obtained $\text{g-C}_3\text{N}_4$ nanosheets in p-gCN-NS sample were ultrathin. In addition, EDS analysis shows that the main elements in p-gCN-NS sample were C and N, which distributed homogeneously in p-gCN-NS (Fig. S1). Cl, as well as other elements, could be negligible in the p-gCN-NS sample, as the peak intensity of Cl was very weak in the EDS (Fig. S1e).

AFM measurement (Fig. 4) shows that the transverse size of $\text{g-C}_3\text{N}_4$ nanosheets in p-gCN-NS was 20–500 nm, the thickness was 2.7–8.7 nm, and the average thickness was about 6 nm, which were consistent with the results of SEM and TEM. Through XRD analysis and all the above morphologic characterization, it is concluded that preparation of $\text{g-C}_3\text{N}_4$ nanosheets by this method was feasible.

Formation mechanism for the special microstructure of p-gCN-NS, $\text{g-C}_3\text{N}_4$ composed of nanosheets and pores is shown in Fig. 5. The pristine melamine particles were sphere-like with smooth surface (Fig. 5a). After acid treatment, many

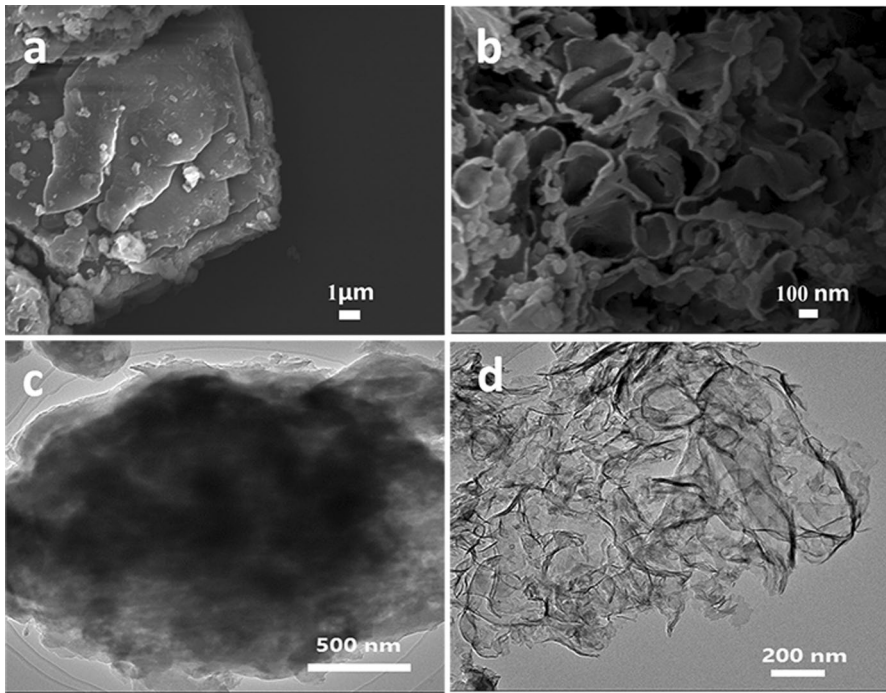


Fig. 3 SEM images of gCN (a) and p-gCN-NS (b), TEM images of gCN (c) and p-gCN-NS (d)

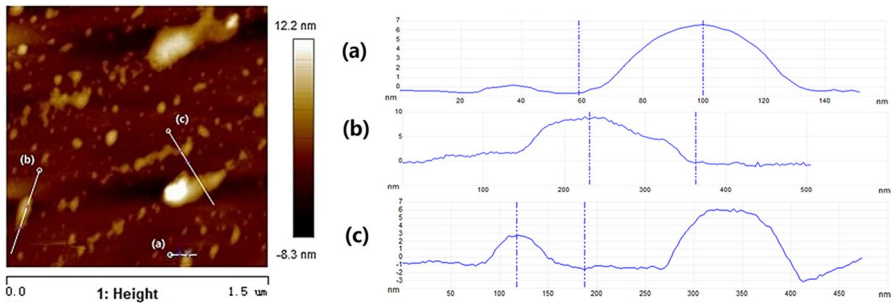


Fig. 4 AFM images of p-gCN-NS sample

fissures appeared on the surface of melamine particles (Fig. 5b) due to the reaction between the amino groups in melamine and the hydrochloric acid molecules. Therefore, when NH_4Cl particles were mixed and ground with the acid-treated melamine particles, they were easily embedded into these fissures (Fig. 5c). Obviously, the obtained mixture of melamine and NH_4Cl in this work was more homogeneous than that reported in literatures [50, 51]. When the mixture was heated at 550°C , a large amount of gas bubbles were generated due to the decomposition

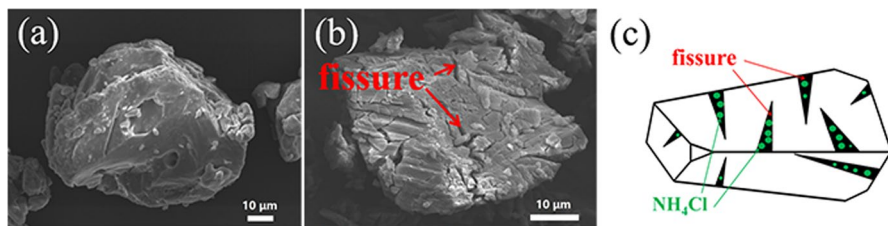


Fig. 5 SEM images of pristine melamine (a), melamine acid-treated for 2 h (b) and the schematic diagram of ammonium chloride particles embedded in fissures of acid-treated melamine after grinding together (c)

of NH_4Cl . As NH_4Cl particles were in a semi-closed or fully closed state in the fissures of melamine, porous nanosheet $\text{g-C}_3\text{N}_4$ were prepared in this study.

Chemical states and elemental composition analysis

Figure 6 and Table 1 exhibit the elemental composition and chemical states of gCN and p-gCN-NS measured by XPS. gCN and p-gCN-NS mainly contained C and N

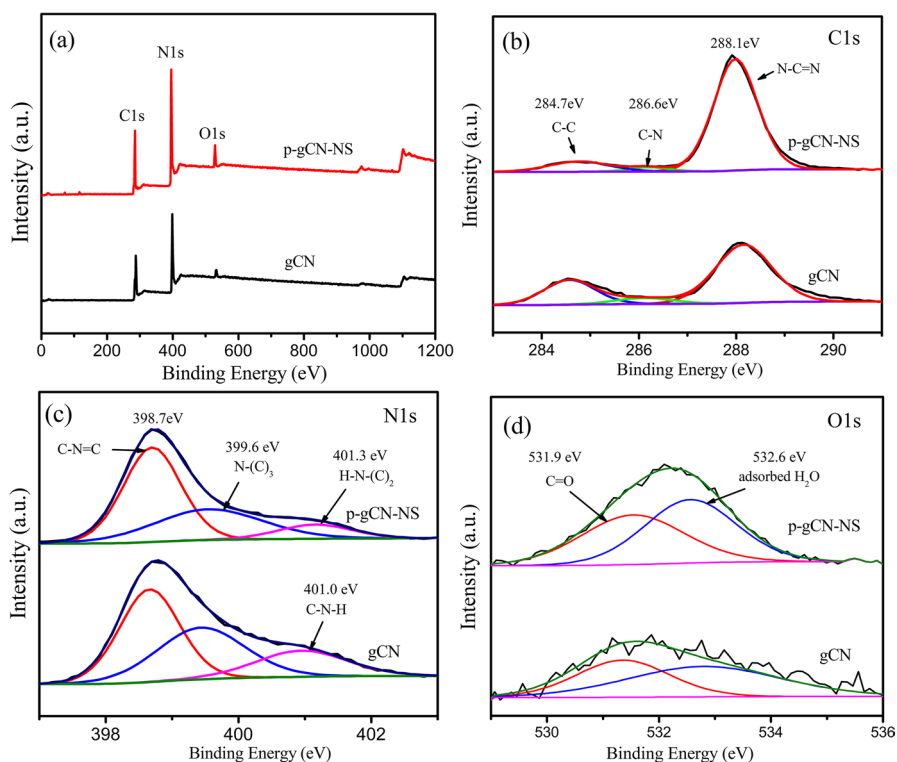


Fig. 6 XPS spectra (a) and high-resolution C 1 s (b), N 1 s (c) and O 1 s (d) spectra of p-gCN-NS and gCN

Table 1 Elemental analysis of gCN and p-gCN-NS

Sample	C (%)	N (%)	O (%)	C/N
gCN	37.94	57.42	4.64	0.66
gCN-NS	41.84	51.79	6.40	0.80

elements, and a small amount of O (Fig. 6a). No Cl-related signals were found in XPS spectrum of p-gCN-NS, suggesting that Cl was not introduced into the structure of g-C₃N₄.

The high-resolution C1s, N1s and O1s spectra of gCN and p-gCN-NS were studied in detail by XPS peak-differentiation-imitating analysis. For C1s spectrum (Fig. 6b), the peaks at 284.7, 286.6 and 288.1 eV were the results of the carbon atoms in C–C bond or impurity, in C–N bond of the aromatic ring and in N–C=N bond of the sp²-hybridized carbon, respectively [44]. The peak intensity of p-gCN-NS at 288.1 eV is stronger than that of gCN, suggesting that N atoms were introduced into the molecular structure of p-gCN-NS [37]. The N1s spectrum (Fig. 6c) was fitted into peaks at about 398.7, 399.5 and 401.0 eV, corresponding to the N atoms in C–N=C bonds of the tri-s-triazine units, N–(C)₃ groups and C–N–H groups, respectively. The electron density of N atoms in p-gCN-NS decreased with the peak position of the N–(C)₃ group moving toward higher energy. This phenomenon implies the existence of sheet structure in p-gCN-NS [52]. The H–N–(C)₂ group occurred at 401.3 eV in the XPS spectrum of p-gCN-NS (Fig. 6c) manifests that the triazine rings were mainly connected by two-coordinated bridging nitrogen [53]. Compared to that in gCN, the peak intensity of N–(C)₃ group in p-gCN-NS was significantly decreased. Besides, the N content in p-gCN-NS decreased, and therefore, the C/N mass ratio increased from 0.66 in gCN to 0.80 in p-gCN-NS (Table 1). As a result, nitrogen vacancies may appear in p-gCN-NS. The O1s spectra of gCN and p-gCN-NS (Fig. 6d) were fitted to two peaks at 531.9 and 532.6 eV, corresponding to the C=O bond and the H₂O molecule adsorbed on the sample surface, respectively. The O1s peak intensity of p-gCN-NS is stronger than that of gCN, which was derived from the increased amount of adsorbed oxygen molecules due to the enhanced specific surface area of p-gCN-NS.

Specific surface area and pore structure analysis

On the basis of IUPAC classification, gCN and p-gCN-NS display adsorption–desorption isotherms of type IV and exhibit H3 hysteresis loops (Fig. 7). The BJH pore size distribution curves (embedded in Fig. 7) illustrate that the pore size of gCN and p-gCN-NS sample was between 1 and 200 nm. However, the pore volume of p-gCN-NS was much higher than that of gCN, and there were a few micropores in p-gCN-NS.

The SSA of p-gCN-NS was 63.65 m²·g^{−1}, which is 6.7 times as much as that of gCN (9.54 m²·g^{−1}). This result was primarily ascribed to the emergence of nanosheets and porous structure in p-gCN-NS. Acid pre-treating of melamine and the addition of NH₄Cl led to the emergence of g-C₃N₄ nanosheets, and the later

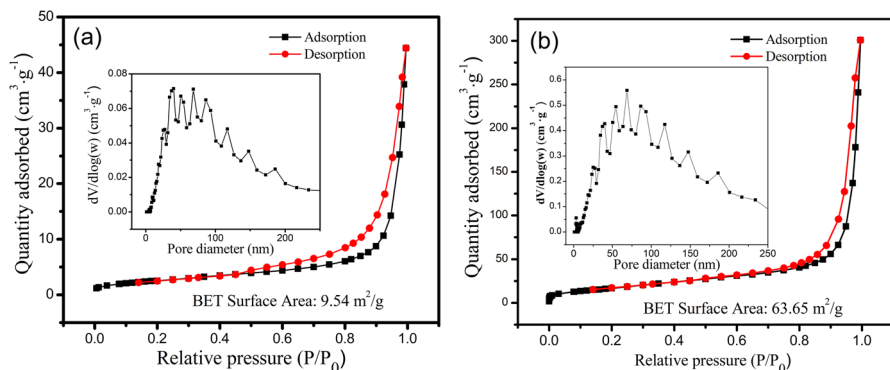


Fig. 7 Nitrogen adsorption–desorption isotherm, BJH pore size distribution curve (embedded graph) and BET surface area of gCN (a) and p-gCN-NS (b)

mainly accounted for the appearance of pores owing to the decomposition of NH₄Cl into gas during the calcination process of p-gCN-NS.

Optical properties

The UV–Vis diffuse reflectance spectra reflect the optical properties of gCN and p-gCN-NS samples (Fig. 8a). Although the absorption edges of gCN and p-gCN-NS were approximately 450 nm, the absorption intensity of p-gCN-NS was stronger than that of gCN in most visible wavelength range. This phenomenon demonstrates that the visible light-harvesting ability of p-gCN-NS was stronger than that of gCN, which may be attributed to the larger SSA and porous structure of p-gCN-NS and the multiple reflection effects. Furthermore, the absorption edge of p-gCN-NS displays a slight blueshift to short wavelength compared to that of gCN. The band gap energy of p-gCN-NS was higher than that of gCN (Fig. 8b), in agreement with the slight blueshift of p-gCN-NS, similar to the previous studies [35].

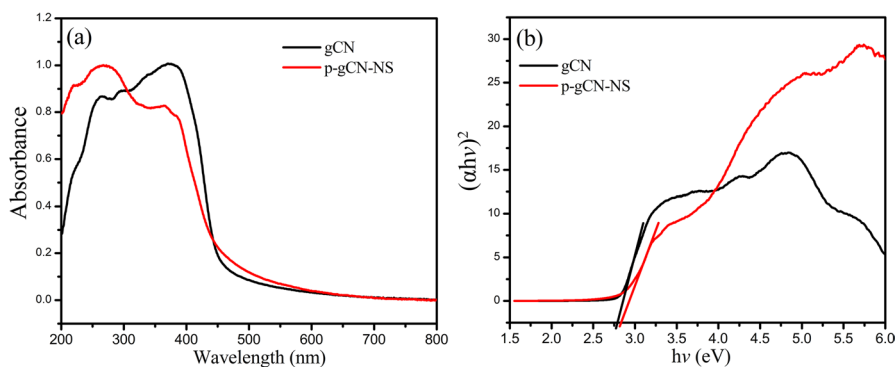


Fig. 8 UV–Vis diffuse reflectance spectra (a) and band gaps (b) of gCN and p-gCN-NS

PL analysis

Charge separation efficiency of the photocatalyst can be obtained from PL spectroscopy since the recombination of photogenerated electrons and holes could give out light. Figure 9a presents the PL spectra of gCN and p-gCN-NS. Evidently, the PL emission intensity of p-gCN-NS was much lower than that of gCN, indicating that the recombination rate of photogenerated electron–hole pairs in p-gCN-NS was significantly lower than that in gCN [54, 55]. This phenomenon may be due to that the reduced g-C₃N₄ thickness in p-gCN-NS shortened the migration path of photogenerated electron–holes; in other words, the photogenerated electron–holes could quickly migrate to the surface of g-C₃N₄. As a result, their recombination rate decreased and resulted in the low PL intensity.

In addition, the emission peak of p-gCN-NS shifted to lower wave number compared with that of gCN. The emission peak of p-gCN-NS was deconvoluted and obtained a sharp emission peak at about 450 nm and a broad emission peak at about 500 nm, which were related to the pathway of $\pi^*-\pi$, π^* –one pair transitions, respectively [56].

Photocatalytic degradation performances of gCN and p-gCN-NS

The photocatalytic activity of gCN and p-gCN-NS were evaluated by photocatalytic degrading the RhB aqueous solution (10 mg/L) under visible light irradiation. Figure 10a shows that RhB was gradually degraded by p-gCN-NS with the extension of photocatalytic time. The degradation curves of RhB by gCN and p-gCN-NS are depicted in Fig. 10b. After the dark reaction for 1 h and achieving the adsorption–desorption equilibrium, the removal rate of RhB was 3.31% for gCN but increased to 28.20% for p-gCN-NS, indicating that the adsorption performance of p-gCN-NS was much better than that of gCN. This result was mainly associated with the higher SSA and the pore structure of p-gCN-NS. Moreover, p-gCN-NS presented much better photocatalytic performance than gCN did.

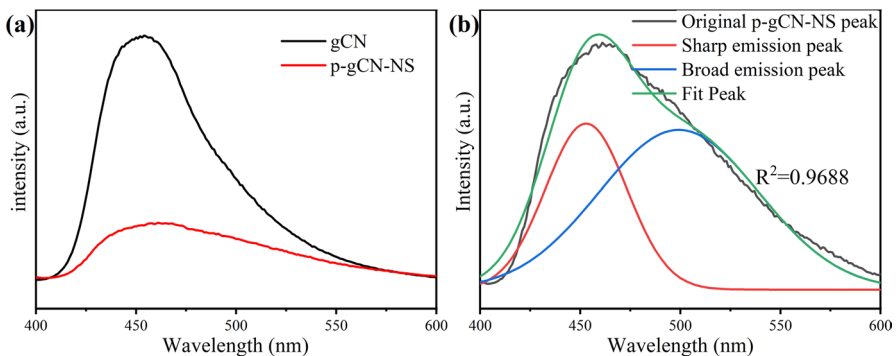


Fig. 9 PL spectra of gCN and p-gCN-NS (a); PL spectra of p-gCN-NS by fitting with deconvoluted integral peak (b)

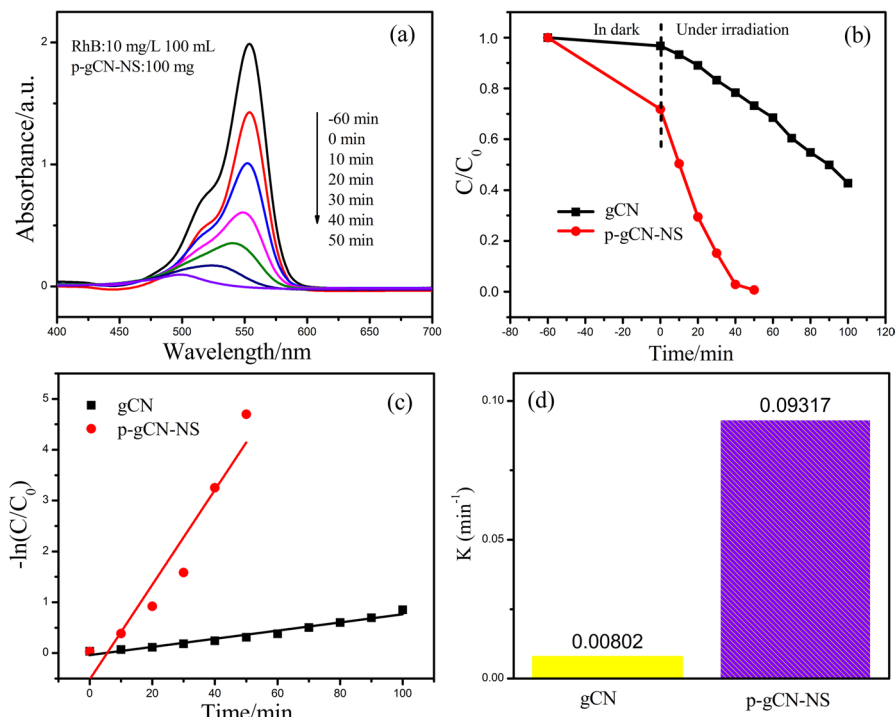


Fig. 10 UV-Vis absorption spectra of the residual RhB solution degraded by p-gCN-NS (a) and the photocatalytic activity (b), first-order kinetic plots for degradation (c) and reaction rate constant (d) of gCN and p-gCN-NS

After photocatalysis for 50 min, the degradation rate of RhB achieved 99.32% by p-gCN-NS, but only got 26.78% by gCN.

The photodegradation of RhB follows the criterion of pseudo-first-order reaction kinetics [45]. Accordingly, the resultant data were fitted on the basis of pseudo-first-order model, and the reaction rate constant (k) was calculated by formula (2):

$$\ln(C/C_0) = -kt \quad (2)$$

where C_0 and C are the initial RhB concentration and the concentration of the RhB solution after reaction time t , respectively. Figure 10c shows the pseudo-first-order kinetic plots as well as the linear fitting for the degradation data, and Fig. 10d gives the k values. p-gCN-NS shows a larger rate constant value ($k=0.09317 \text{ min}^{-1}$), which is 10.6 times higher than that of gCN ($k=0.00802 \text{ min}^{-1}$). Of course, the photocatalytic degradation rates of RhB enhanced with the increasing of p-gCN-NS dosages, but all photocatalytic degradation reaction followed the pseudo-first-order kinetic model (Fig. S2). The improved photocatalytic performance can be credited to the reduced sized and thickness, higher SSA and pore structure, reduced recombination rate of photogenerated electron-hole pairs of p-gCN-NS.

The photocatalytic activity of g-C₃N₄ nanosheets prepared by different methods is compared in Table 2. Under the same experimental conditions, p-gCN-NS exhibited better photocatalytic degradation activity toward RhB than many other samples reported in literatures, as RhB was completely degraded within 50 min by p-gCN-NS in this work. This result indicates that the strategy in this work was feasible to the synthesis of high performances g-C₃N₄ photocatalyst.

Figure S3 exhibits the photocatalytic degradation curves of tetracycline aqueous solution (10 mg/L, 100 mL) by 100 mg gCN and p-gCN-NS under visible light irradiation. It can be seen that the removal rate of tetracycline by the adsorption of p-gCN-NS was much higher than that of gCN after reaching the adsorption–desorption equilibrium under dark reaction. This phenomenon revealed that the amount of adsorption sites in p-gCN-NS was much greater than that in gCN, coinciding with the much larger specific surface area of p-gCN-NS. After photocatalytic reaction for 120 min under visible light irradiation, the degradation rate of tetracycline by gCN was 58.07%, but that by p-gCN-NS achieved as high as 72.01%. This result was similar to the degradation of RhB, which indicates that the as-prepared p-gCN-NS exhibited higher photocatalytic activity not only to color pollutants but also to colorless pollutants.

Under the similar experiment conditions as those photocatalytic degrading RhB, cycle experiment and free radical trapping experiments were carried out by using p-gCN-NS as the photocatalyst. After five cycles of photocatalytic degradation, the degradation rate of RhB by p-gCN-NS decreased from 99.32% to 67.49% (Fig. 11a), which means its performance stability should be improved in the future. During the free radical trapping experiments, isopropanol (IPA), triethanolamine (TEOA) and benzoquinone (BQ) were used as active species scavenger for ·OH, h⁺ and ·O²⁻, respectively. The results (Fig. 11b) show that the photocatalytic activity of p-gCN-NS was slightly affected after the addition of IPA, but significantly inhibited after the addition of TEOA and BQ. These phenomena mean that h⁺ and ·O²⁻ were the main active species for the photocatalytic degradation of RhB by p-gCN-NS.

Table 2 Comparison of photocatalytic degradation properties and SSA of g-C₃N₄ nanosheets prepared by different methods

Preparation method	SSA (m ² ·g ⁻¹)	Photocatalyst dosage (mg)	RhB concentration (mg/L)/volume (mL)	Desired time (min)	Reference
Heating with NH ₄ Cl	No test	100	10/100	120	[42]
Ammonia solution treating	41.1	10	10/10	120	[49]
Facial supramolecular method	79.68	10	10/10	180	[57]
Direct condensation	109.9	50	10/100	60	[58]
Acid treating melamine and heating with NH ₄ Cl	63.65	100	10/100	50	This work

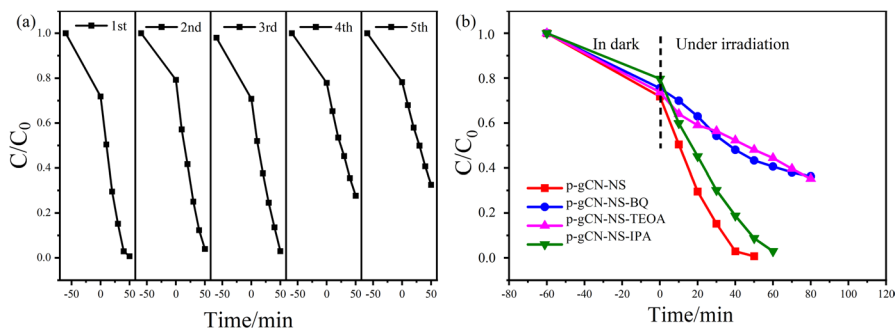


Fig. 11 Photocatalytic degradation curves of RhB by p-gCN-NS. (a) Cycle experiments. (b) Free radical trapping experiments

Conclusion

In summary, porous $g\text{-C}_3\text{N}_4$ composed of nanosheets with excellent photocatalytic performance was successfully prepared by firstly pre-treating melamine with hydrochloric acid and then grinding and calcining with NH_4Cl at 550°C for 2 h. The crystallinity, size and thickness of $g\text{-C}_3\text{N}_4$ in p-gCN-NS had a great drop, and the average thickness of $g\text{-C}_3\text{N}_4$ was about 6 nm. SSA of p-gCN-NS was $63.65\text{ m}^2\cdot\text{g}^{-1}$, which was 6.7 times that of gCN. The unique microstructure of p-gCN-NS was mainly ascribed to that NH_4Cl particles were embedded in fissures of the acid-treated melamine particles. p-gCN-NS possessed excellent photocatalytic activity compared to gCN. After photocatalysis for 50 min, the degradation rate of RhB aqueous solution (10 mg/L, 100 mL) achieved 99.32% by p-gCN-NS (100 mg), whose reaction rate constant ($k=0.09317\text{ min}^{-1}$) was 10.6 times higher than that of gCN. p-gCN-NS also exhibited excellent photocatalytic activity to the degradation of colorless tetracycline aqueous solution. This work provides a feasible and facile method for the preparation of porous $g\text{-C}_3\text{N}_4$ composed of nanosheets with excellent photocatalytic performance.

Supplementary Information The online version contains supplementary material available at <https://doi.org/10.1007/s11164-023-05030-6>.

Author contributions TH and SS were involved in investigation, material preparation, data collection and analysis, and writing the original draft. HX was responsible for conceptualization, methodology, supervision, project administration, review and editing. Han Yu took part in material preparation and data analysis. WC contributed to investigation and methodology. GS, BF, HW and HL participated in methodology and review. All authors read and approved the final manuscript.

Funding We would like to express our gratitude to Henan Province Natural Science Foundation, China (grant number 212300410407) and the Key Science and Technology Research Project of Henan province, China (grant numbers 182102210005) for their supports to this work.

Data availability The datasets generated during and/or analyzed during the current study are available from the corresponding author on reasonable request.

Declarations

Competing interests There are no conflicts of interest to declare.

Ethical approval Not applicable.

References

1. G. Liu, X. Qiao, M.A. Gondal, Y. Liu, K. Shen, Q. Xu, J. Nanosci. Nanotechnol. **18**, 4142 (2018)
2. L. Lei, W. Wang, W. Yu et al., Res. Chem. Intermed. **46**, 4673 (2020)
3. Y. Chang, Z. Liu, X. Shen, B. Zhu, D.K. Macharia, Z. Chen, L. Zhang, J. Hazard. Mater. **344**, 1188 (2018)
4. H. Xu, Z. Wu, Y. Wang, C. Lin, J. Mater. Sci. **52**, 9477 (2017)
5. J. Schneider, M. Matsuoka, M. Takeuchi, J. Zhang, Y. Horiuchi, M. Anpo, D.W. Bahnemann, Chem Rev. **114**(19), 9919 (2014)
6. J. Yu, J. Lei, L. Wang et al., Res. Chem. Intermed **45**, 4237 (2019)
7. L. Jing, W.-J. Ong, R. Zhang, E. Pickwell-MacPherson, J.C. Yu, Catal. Today **315**, 103 (2018)
8. B. Wang, M. Anpo, X. Wang, Adv. Inorg. Chem. **72**, 49 (2018)
9. G. Li, J. Shi, G. Zhang et al., Res Chem Intermed **43**, 5137 (2017)
10. A. Hayat, Z. Chen, Z. Luo et al., Res Chem Intermed **47**, 15 (2021)
11. X. Huang, W. Gu, Y. Ma et al., Res. Chem. Intermed. **46**, 5133 (2020)
12. J. Tian, Q. Liu, C. Ge, Z. Xing, A.M. Asiri, A.O. Al-Youbi, X. Sun, Nanoscale **5**, 8921 (2013)
13. E.I. García-López, Z. Abbasi, F. Di Franco et al., Res. Chem. Intermed. **47**, 131 (2021)
14. F. Chen, M. Yang, X. Shi et al., Res Chem Intermed **49**, 101 (2023)
15. L. Jiang, X. Yuan, G. Zeng, Z. Wu, J. Liang, X. Chen, L. Leng, H. Wang, H. Wang, Appl. Catal. B-Environ. **221**, 715 (2018)
16. H. Miao, G. Zhang, X. Hu, J. Mu, T. Han, J. Fan, C. Zhu, L. Song, J. Bai, X. Hou, J. Alloys Compd. **690**, 669 (2017)
17. P. Wang, C. Guo, S. Hou, X. Zhao, L. Wu, Y. Pei, Y. Zhang, J. Gao, J. Xu, J. Alloys Compd. **769**, 503 (2018)
18. X. Chen, J. Zhang, X. Fu, M. Antonietti, X. Wang, J. Am. Chem. Soc. **131**(33), 11658 (2009)
19. Q. Zhang, X. Gao, Y. Wang, H. Li, Y. Zhang, Y. Fan, J. Niu, Mater. Sci. Semicond. Process **104**, 104689 (2019)
20. S. Guo, Z. Deng, M. Li, B. Jiang, C. Tian, Q. Pan, H. Fu, Angew. Chem. Int. Ed. **55**, 1830 (2016)
21. L. Ge, C. Han, X. Xiao, L. Guo, Y. Li, Mater. Res. Bull. **48**, 3919 (2013)
22. J. Zhang, X. Chen, K. Takanebe, K. Maeda, K. Domen, J.D. Epping, X. Fu, M. Antonietti, X. Wang, Angew. Chem. Int. Ed. Engl. **49**(2), 441 (2010)
23. T. Yu, Z. Hu, H. Wang, X. Tan, J. Mater. Sci. **55**, 2118 (2020)
24. H. He, L. Huang, Z. Zhong, S. Tan, Appl. Surf. Sci. **441**, 285 (2018)
25. T. Song, P. Zhang, T. Wang, A. Ali, H. Zeng, Appl. Catal. B-Environ. **224**, 877 (2018)
26. S.-W. Bian, Z. Ma, W.-G. Song, J. Phys. Chem. C **113**, 8668 (2009)
27. Z. Mo, H. Xu, Z. Chen, X. She, Y. Song, J. Wu, P. Yan, L. Xu, Y. Leia, S. Yuan, H. Li, Appl. Catal. B-Environ. **225**, 154 (2018)
28. J. Liu, J. Huang, H. Zhou, M. Antonietti, ACS Appl. Mater. Interfaces. **6**, 8434 (2014)
29. Q. Liang, Z. Li, Z.-H. Huang, F. Kang, Q.-H. Yang, Adv. Funct. Mater. **25**, 6885 (2015)
30. G. Li, L. Li, H. Yuan, H. Wang, H. Zeng, J. Shi, J. Colloid Interface Sci. **495**, 19 (2017)
31. H. Huang, K. Xiao, N. Tian, F. Dong, T. Zhang, X. Du, Y. Zhang, J. Mater. Chem. A **5**, 17452 (2017)
32. D.-F. Li, W.-Q. Huang, L.-R. Zou, A. Pan, G.-F. Huang, J. Nanosci. Nanotechnol. **18**, 5502 (2018)
33. F. Dong, Y. Li, Z. Wang, W.-K. Ho, Appl. Surf. Sci. **358**, 393 (2015)
34. X. Lu, K. Xu, P. Chen, K. Jia, S. Liu, C. Wu, J. Mater. Chem. A **2**, 18924 (2014)
35. H. Xu, J. Yan, X. She, L. Xu, J. Xia, Y. Xu, Y. Song, L. Huang, H. Li, Nanoscale **6**, 1406 (2014)
36. J. Ma, X. Tan, F. Jiang, T. Yu, Catal. Sci. Technol. **7**, 3275 (2017)
37. B. Fei, Y. Tang, X. Wang, X. Dong, J. Liang, X. Fei, L. Xu, Y. Song, F. Mater. Res. Bull. **102**, 209–217 (2018)

38. X. Wang, K. Maeda, X. Chen, K. Takanahe, K. Domen, Y. Hou, X. Fu, *M. J. Am. Chem. Soc.* **131**(5), 1680 (2009)
39. Sun Shiping, Erchuang et al., *J. Nanotechnol.* **30**, 315601 (2019)
40. L. Huang, Y. Li, H. Xu, Y. Xu, J. Xia, K. Wang, H. Li, X. Cheng, *Rsc Adv.* **3**, 22269 (2013)
41. Y. Hong, C. Li, D. Li, Z. Fang, B. Luo, X. Yan, H. Shen, B. Mao, W. Shi, *Nanoscale* **9**, 14103 (2017)
42. J. Xu, L. Zhang, R. Shi, Y. Zhu, *J. Mater. Chem. A* **1**, 14766 (2013)
43. X. Wang, K. Maeda, A. Thomas, K. Takanahe, G. Xin, J.M. Carlsson, K. Domen, M. Antonietti, *Nat. Mater.* **8**(1), 76 (2009)
44. T.Y. Ma, Y. Tang, S. Dai, S.Z. Qiao, *Small* **10**, 2382 (2014)
45. J. Yan, C. Zhou, P. Li, B. Chen, S. Zhang, X. Dong, F. Xi, J. Liu, *Colloids Surf. Physicochem. Eng. Asp.* **508**, 257 (2016)
46. S. Thaweesak, M. Lyu, P. Peerakiatkhajohn, T. Butburee, B. Luo, H. Chen, L. Wang, *Appl. Catal. B-Environm.* **202**, 184 (2017)
47. L. Ma, H. Fan, J. Wang, Y. Zhao, H. Tian, G. Dong, *Appl. Catal. B-Environ.* **190**, 93–102 (2016)
48. X.-H. Song, L. Feng, S.-L. Deng, S.-Y. Xie, L.-S. Zheng, *Adv. Mater. Interfaces* **4**(15), 1700339 (2017)
49. L.J. Fang, Y.H. Li, P.F. Liu, D.P. Wang, H.D. Zeng, X.L. Wang, H.G. Yang, *Acs. Sustain. Chem. Eng.* **5**, 2039 (2017)
50. W. Iqbal, B. Qiu, J. Lei, L. Wang, J. Zhang, M. Anpo, *Dalton Trans.* **46**, 10678 (2017)
51. J. Gao, Y. Wang, S. Zhou, W. Lin, Y. Kong, *ChemCatChem* **9**, 1708 (2017)
52. C. Fan, J. Miao, G. Xu, J. Liu, J. Lv, Y. Wu, *RSC Adv.* **7**, 37185 (2017)
53. G. Dong, W. Ho, Y. Li, L. Zhang, *Appl. Catal. B-Environ.* **174**, 477 (2015)
54. Q. Li, M. Anpo, X. Wang, *Res. Chem. Intermed.* **46**, 4325 (2020)
55. P. Yang, J. Zhao, W. Qiao, L. Li, Z. Zhu, *Nanoscale* **7**(45), 18887 (2015)
56. X. Zhang, S.P. Jiang, P. Yang, *J. Lumin.* **235**, 118055 (2021)
57. S. Wan, M. Ou, Q. Zhong, S. Zhang, W. Cai, *Adv. Opt. Mater.* **5**, 23 (2017)
58. Z. Huang, F. Li, B. Chen, G. Yuan, *Catal. Sci. Technol.* **4**, 4258 (2014)

Publisher's Note Springer Nature remains neutral with regard to jurisdictional claims in published maps and institutional affiliations.

Springer Nature or its licensor (e.g. a society or other partner) holds exclusive rights to this article under a publishing agreement with the author(s) or other rightsholder(s); author self-archiving of the accepted manuscript version of this article is solely governed by the terms of such publishing agreement and applicable law.